

Toward a practical appraisal for waveform tomography of band- and offset-limited marine seismic data

Clàudia Gras, Clara Estela Jiménez-Tejero, Valentí Sallarès, Adrià Meléndez, and César R. Ranero

Abstract—We present a generalized workflow to retrieve high-resolution P-wave velocity (V_P) models of complex Earth's subsurface structures from traditional marine near-vertical seismic reflection experiments. These records have typically offsets too short to map refraction phases and lack low frequency information. The workflow is composed of three steps: (1) downward continuation (DC) of seismic records to the seafloor to recover diving wave information; (2) travel-time tomography (TTT) of first arrivals obtained from DC data, to retrieve a kinematically correct model, and (3) full-waveform inversion (FWI) of the original streamer data set, starting with the model obtained with TTT and sequentially introducing higher wavenumber details into the model. We show that the TTT allows overcoming the issues associated to the non-linearity intrinsic to FWI. We also disentangle envelope and phase from the waveform to choose the objective function most suitable for FWI. We assess the accuracy of initial models and predict the quality of the FWI results by quantifying the early-arrival cycle skipping between original and simulated data. The efficiency of the workflow is tested with a challenging synthetic target model, containing vertical boundaries with a strong velocity contrasts and velocity inversions embedded in a checkerboard-like pattern. We show that workflow steps (1) and (2) provide a TTT model that is not cycle-skipped at the frequencies available in most marine seismic experiments, and thus allow step (3) FWI to obtain high-resolution V_P models of the subsurface using band- and offset-limited field data sets, traditionally collected in marine airgun and streamer acquisitions.

Index Terms—Acoustic waves, Downward continuation, Full waveform inversion, Inverse theory, Marine seismic data, Numerical modelling, Signal analysis, Travel time tomography, Velocity models, Waveform tomography.

I. INTRODUCTION

A. Seismic acquisition systems

IMAGINING the Earth's interior with seismic waves is challenging due to the intricate interactions between multiple factors that affect wave propagation and the imperfect simulation of the related physical phenomena. Subsurface geology contains variable degrees of complexity at different scales, and different seismic imaging techniques are designed to map the particular attributes of the seismic wavefield that

are most relevant at the different scales. Marine seismic data routinely acquired by both industry and academia are recorded with hydrophone streamers with lengths ranging from 2.4 to 6 km for vintage data, to 6 to 9 km in modern data. In most circumstances, with water layers of 1-5 km and sub-seafloor targets of 1-15 km means that nearly all recorded arrivals correspond to a near-vertical acquisition, i.e. offsets shorter than the critical distance to record refractions. This acquisition system, denoted in academia as multi-channel seismic reflection (MCS), is well suited to record the reflectivity at geological boundaries. Most MCS streamer systems record near-vertical reflections at short offsets with high redundancy and lateral sampling, being able to image small-scale features at shallower depths. However, because reflected phases are subject to trade-offs between reflector location and the velocity field above it, the MCS streamer data are not well-suited to extract high-resolution velocity information. Thus, MCS records are commonly used to construct laterally continuous images of the subsurface geological layering in two-way time, but provide limited information of the velocity field. The subsurface V_P structure can be more accurately obtained from diving waves, but these appear after the critical angle at offsets that are typically longer than most streamer records. Fig. 1a shows eight vertical V_P /depth profiles that represent the inferior and superior limits (i.e. the smoothest and strongest V_P gradients with depth) of a compilation of V_P /depth profiles for four different geological domains; igneous oceanic crust [57], exhumed mantle [42], [49], magmatic crust [24], and sedimentary basin deposits [43]. Using these V_P limits, we show in Fig. 1b how the maximum experimental depth reached by ray tracing of refracted phases varies depending on the maximum acquisition offset (maximum source-receiver separation). The deepest penetration of first arrivals is reached for larger acquisition offsets in the areas with comparatively smoother V_P gradients (Fig. 1a).

B. Seismic data inversion

The difficulty of characterizing the physical properties of the subsurface from seismic records has promoted a long standing effort to develop seismic modelling techniques. Many methods have been developed to describe the seismic-wave propagation, including those reproducing travel-times by ray tracing (e.g. [27], [32], [60]) or more complete attributes of the wavefield using the wave equation ([33], [53]).

Modern inverse modelling techniques aim at fitting the data in an objective and automatic way. The automatic inversion

C. Gras, C. E. Jiménez-Tejero, V. Sallarès and A. Meléndez are with the Barcelona Center for Subsurface Imaging (Barcelona-CSI), Institute of Marine Science (ICM), Spanish National Research Council (CSIC), 08003 Barcelona, Spain, e-mails: (gras@icm.csic.es, ejimenez@icm.csic.es, vsallarès@icm.csic.es and adria.melendez.catalan@gmail.com, respectively).

C.R. Ranero is with ICREA, Passeig de Lluís Companys, 23, 08010, Barcelona, Spain, and the Barcelona-CSI, ICM, CSIC, 08003 Barcelona, Spain, e-mail: (cranero@cmima.csic.es).

Manuscript received September 24, 2020; revised , 2020.

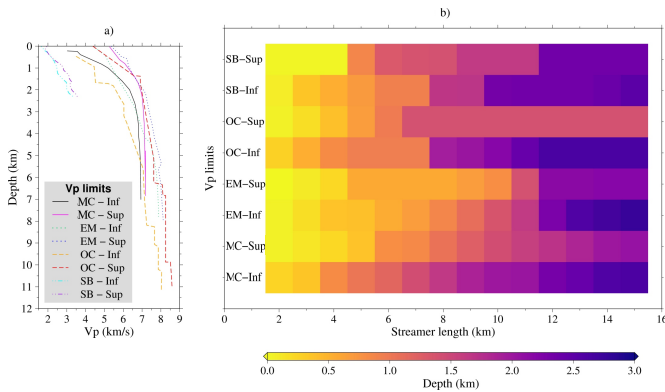


Fig. 1. (a) V_P /depth profiles that represent the inferior (Inf.) and superior (Sup.) limits (i.e. the smoothest and highest V_P gradients in depth) of a compilation of V_P /depth profiles for four different geological domains: magmatic crust (MC) (solid line) [24], exhumed mantle (EM) (dotted line) [42], [49], oceanic crust (OC) (dashed line) [57], and sedimentary basin (SB) (dotted and dashed line) [43]. (b) The maximum depth reached by refracted phases depending on the streamer length (X axis, maximum source-receiver separation) and the velocity gradient of the media (Y axis, V_P /depth limits in (a)). The color scale represents depth in km. The deepest penetration of first arrivals is reached for larger acquisition offsets in the areas with comparatively smoother V_P gradients.

of V_P distribution and geometry of reflectors may use travel-time information of refractions, reflections or both events in a joint tomography. Because TTT methods are focused on fitting only travel-time information, they are moderately nonlinear and robust, however of limited resolution, determined by the size of the first Fresnel zone approximated by $\sim \sqrt{\lambda \cdot L}$ [58], where λ is the source wavelength and L the source-receiver propagation distance. Increasing computational resources has prompted the development of increasingly complex FWI techniques that aim to fit a suit of wave attributes other than travel-times (e.g. [13], [16], [38], [44]). FWI uses some expression of the wave equation to simulate the full wave propagation and to retrieve the seismic wavefield at receiver locations. To do it, an inverse problem is set to define the model of physical properties that fits the observations. The main advantage of FWI compared to TTT is that it provides higher-resolution models, potentially around a half of the propagation wavelength ($\lambda/2$). However, FWI is highly nonlinear, and requires data containing frequencies as low as 0.5-1.0 Hz. Otherwise, there is usually a frequency gap between the initial and recorded data that increases the non-linearity and the poor performance of FWI. The problem occurs when recorded and the simulated wavefields are out of phase by more than half a period, causing cycle-skipping and preventing FWI to retrieve a kinematically correct initial model containing the low-wavenumber information [14]. Most field data lack frequencies < 4 -5 Hz, so FWI requires using complementary techniques to build kinematically-correct velocity models that allow to fill the frequency gap and overcoming cycle-skipping. In the absence of a priori information, the efforts have been focused on retrieving the low wavenumbers masked in the data set (e.g. [17], [29]), to employ more robust objective functions to compare the recorded and simulated wavefield (e.g. [2], [30], [31], [59]) or to implement signal- and/or gradient-based

preconditioning or regularization techniques (e.g. [3], [55]). A variety of strategies combining different tomographic methods, and in particular TTT and FWI, have been proposed to overcome cycle-skipping in MCS data inversion (e.g. [9], [22], [48]). However, some of these have been shown useful only in particular experimental conditions (i.e. large offsets, low noise ratio, laterally homogeneous media, etc.), and may be insufficient to overcome cycle-skipping issues as a generalist approach. Given these difficulties, FWI is usually considered applicable to only a few data sets, and unfeasible especially in limited-offset deep water MCS acquisition geometries.

Here we present a study with synthetic data to illustrate the inadvertent potential associated to the combined TTT+FWI approach, and we propose a generalized workflow and associated tests to successfully apply it to most marine streamer MCS data. The applicability of the workflow is tested with synthetic data to compare inverted and real models and analyze the results after each workflow step. We first recover the early refractions as first arrivals by downward continuation (DC) [4], [6], [7], [22] if they are masked on MCS shot gathers. The critical offset where refractions appear earlier than reflections in streamer data is $2 \cdot d \cdot (u/w)$, where d is the water depth, $u = v_1/v_2$, and $w = \sqrt{1-u^2}$. Therefore, these variables are key to decide whether to apply DC or not. The downward continued first arrival travel-times are used with TTT to retrieve the low-wavenumber V_P information. We show that it can be done for a variety of acquisition setups, and it does not require the rare ultra-long streamer acquisition [21], [48] or shallow water environments (e.g. [1]). The TTT-inverted V_P model is shown to be kinematically correct, so data modelled are not cycle-skipped at the lowest available frequency of typical marine MCS experiments (4-5 Hz). The resulting V_P field is used as initial model to perform multi-scale FWI [15], in which increasing wavenumber details are progressively incorporated into the model. The study shows that FWI can potentially be used with a wide range of data, including offset- and band-limited marine MCS data when a proper workflow is applied. This study also presents a quantitative and visual approach to assess cycle skipping, which is used as an indicator of the suitability of the initial model and quality of the inversion result.

II. TARGET V_P MODEL AND SIMULATED DATA SET

To evaluate the potential, advantages and drawbacks of the proposed inversion procedure, we have built a complex synthetic model that includes V_P inversions and strong lateral V_P contrasts (Fig. 2a), which are some of the most difficult features to recover. The V_P model displays a background V_P gradient superimposed with a pattern of checkerboard-like anomalies. The model dimensions are ~ 9.5 km long x 3 km deep. For simplicity, a horizontal seafloor is located below a 1 km deep water column with a constant V_P of 1.5 km/s. The background V_P gradient is $V_P(z) = 1.5 + 1.25 \cdot z$ (km/s), where z is depth, going from 1.5 km/s at the seafloor to 4 km/s at the bottom of the model. The dimensions of the checkerboard anomalies are 1.5 km wide x 0.75 km deep between the seafloor and 0.75 km depth, and 2.25 km wide x

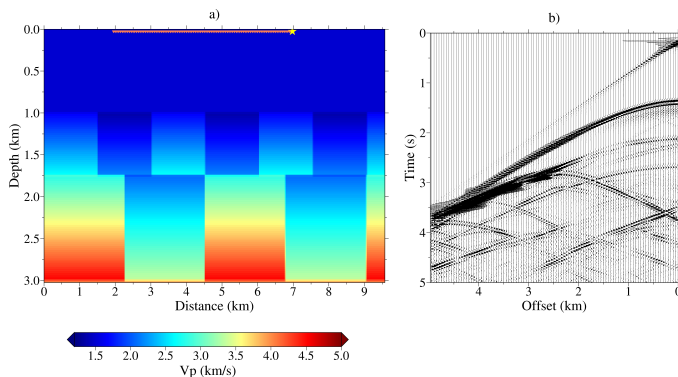


Fig. 2. (a) The target 2-D checkerboard V_P model, which includes a 1 km deep water layer above a checkerboard-type model, with larger-size anomalies in the deeper part than in the upper part; superimposed on a vertical V_P gradient. The color scale represents V_P in km/s. (b) Data simulated with the parameterization and acquisition geometry described in the text. The shot is located at a distance of 6.975 km along model and it is plotted in (a) as a yellow star. Receiver positions are plotted as orange reverse triangles in (a).

1.25 km deep from 0.75 km depth to the bottom of the model. The checkerboard anomalies have an amplitude of $\pm 10\%$ with respect to the background V_P in the shallow part, and of $\pm 15\%$ in the deeper part. Additional information is provided in the Supplementary material (S1).

Our goal here is to retrieve the V_P model shown in Fig. 2a with the highest possible accuracy and resolution without a priori information and using limited-offset MCS data alone. Thus, the synthetic experiment simulates a marine MCS survey with a 5-km long streamer, which is a standard streamer length for conventional marine surveys. The simulated streamer has 100 channels, separated 50 m from each other. The source is located 75 m ahead of the first channel. Sources and receivers are located at a depth of 25 m. A total of 45 shots with a central frequency of ~ 8 Hz, starting at 5.075 km from the left boundary spaced 100 m from each other towards the right, are used to simulate the target data set (Fig. 2b). To simulate the V_P wave propagation the target V_P field is parameterized using a regular mesh with 12.5 m node spacing, both vertically and laterally, perfect matched layer (PML) boundary conditions to avoid spurious reflections on the left, right, and bottom boundaries of the model, and a free surface boundary condition on top, that represents the water surface boundary. The simulation time is 8 s and the time sampling is 1.4 ms. The combination of a limited offset acquisition and a relatively deep water column makes that early arrivals in the streamer recordings are dominated by shallow near-vertical reflections (see Fig. 2b). Arrivals from refractions or diving waves are masked by these shallow reflections throughout most of the shotgathers.

III. DATA MODELLING WORKFLOW

The workflow to obtain high-resolution images of the subsurface consists on applying: (A) downward continuation (DC), (B) first arrival travel-time tomography (TTT) and (C) full-waveform inversion (FWI). In the next sections, we explain the basics and main motivation of each step and show the corresponding test results. We also show the FWI results

obtained without following the proposed workflow with and without low wavenumber information on the data set.

A. Downward Continuation

The DC allows simulating an experiment set up that is equivalent to the real one but recorded at a virtual surface. This can be properly done when we have a good approximation of the velocity model of the system between the real and the virtual acquisition surface, such as the velocity of the water column. In the case of marine MCS data the surface is often the seafloor (seafloor-type geometry), so that the model to simulate the propagation is the water column [4], [6], [7], [22]. The main goal of DC is to unmask the first arrivals or early refractions to be used afterwards to retrieve information of the subsurface V_P field. In this section, we analyze the accuracy of the method by comparing the results with simulated data using the target V_P model and the virtual, downward-continued geometry set up.

Prior to DC, in this synthetic case, the only data pre-conditioning step consists on muting the direct arrival as this energy has no information on the subsurface properties. To do so, we simulate the direct arrival through the water column, and then the result is subtracted from the shot gathers. In the case of field data, the data pre-conditioning will also focus on shot gather noise filtering. It is important not to change the seismic waveforms so as not to affect the new emergent arrivals during the DC process. Once we have the data ready, we follow the main steps of the DC approach that includes two back-propagations through the water layer, one in the shot gather domain and the other in the receiver gather domain [6], [7]. Although the new virtual source and receiver positions are in a flat surface, our DC solver works for any geometry of the virtual acquisition surface or seafloor relief. Moreover, the effect of a variable water velocity in DC is also taken into account in the solver, because it back-propagates the data through a V_P water model that can be built from oceanographic measurements. Here the inverse extrapolation of the data follows the scheme of [35], [36]. The DC code consists on a finite difference solver in time domain, which is described in [22] together with a practical application in field data. The panel (a) in Fig. 3 shows one example of a downward-continued shot gather and panel (b) shows the corresponding shot gather but simulated by propagating the seismic source in the target model with the sources and receivers at the seafloor.

Most seismic events in Fig. 3b are also displayed in Fig. 3a. Wave amplitudes of the DC shot gather (Fig. 3a) are much smaller than the simulated ones (Fig. 3b), because of the energy lost during the two back-propagations (sources and receivers) that are done during the DC. Fig. 3b is displayed with lower gain so that reflections are less clear because of the high-amplitude event that corresponds to the direct wave. Aside from wave amplitudes, differences arise from the direct arrival and the sea surface reflection, both present only in Fig. 3b. As the water and the shallow subsurface velocities are similar, the direct wave that travels through the water column and the one that travels through the subsurface have

similar slopes so they appear superimposed as first arrivals in the first 2.5 km of offset distance. Also, the sea surface reflection is located at ~ 1.5 s at zero offset in Fig. 3b. Another difference is that the DC shot gather (Fig. 3a) shows energy arriving before the first arrival. This artifact forms during the extrapolation process as part of the wave back-propagation. The magnitude of this artifact is amplified if there are aliasing effects, caused by the discrete sampling of the wavefield used as input for the DC extrapolations. Sparse seismic acquisition with large distances between sources and/or receivers produce less focused wavefields and, therefore, it is more likely to get aliasing-related effects.

Regardless of artifacts, the downward-continued shotgather display clear early refractions from the shallow subsurface (Fig. 3a), that were obscured in the original recordings (Fig. 2b). The fact that sources and receivers are both now located at the seafloor allows to track the first arrivals from zero offset to the end of the streamer length (blue dots in Fig. 3c-d). However, first arrivals are more difficult to identify at long offsets, due to amplitude attenuation and truncation of the seismic records (Fig. 3a). The arrival times simulated with a ray-tracing algorithm [32] are plotted as blue dots in Fig. 3c-d. We can see that travel-times correspond to those obtained from the DC data within ± 0.13 ms on average (Fig. 3a-c). Thus, Fig. 3c demonstrates that first arrival travel times are not significantly affected by the DC so that they should contain proper information on the V_P of the shallow subsurface. Therefore, these phases can then be picked and used as input for TTT.

B. Travel-time Tomography

The goal of this step is to show that a kinetically accurate background macro-velocity model can be retrieved by performing TTT with the first arrivals identified in the downward continued shot gathers. We also analyze the coverage and resolving potential of the first arrival TTT method for a seafloor acquisition-type data configuration (Fig. 4). We use the TOMO2D code [5], [32], [37] to perform the first arrival TTT and obtain the V_P structure of the subsurface. To demonstrate that a kinematically-correct V_P model can be retrieved from the DC picks we use an initial model consisting of a vertical velocity gradient without a prior information.

Fig. 4 shows the first arrival ray paths for this acquisition geometry, which in turn illustrates the model coverage. The target of the TTT is to retrieve the V_P information from the travel times of these rays. The right part is the best-covered zone because the vessel moves towards this direction. It must be noted that the areas of the model with poor ray coverage will be strongly conditioned by the initial model and regularization constraints used. The coverage and number of crossing rays and thus the derivative weight sum [54] strongly decrease with depth, especially in the low- V_P zones. Low- V_P anomalies tend to be avoided by first arrival ray paths. Therefore, in the target model deeper ray trajectories are limited to some high- V_P areas. The ray coverage show that the maximum depth that can be achieved for this model and survey configuration is around 2 km below the seafloor. However,

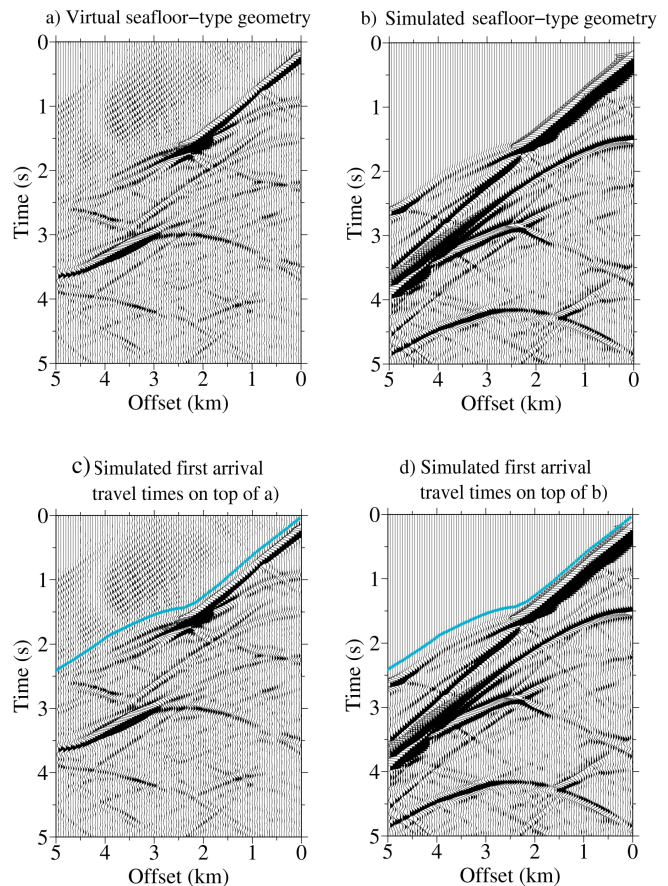


Fig. 3. (a) Seismic data obtained from the DC of the streamer shots simulating a virtual seafloor-type geometry. Shot location is at 6.975 km along the model. (b) Same shot as (a) but generated using the target V_P model and the seafloor-type geometry. Blue dots in (c)-(d) are the first arrival travel times of the shortest ray paths calculated using TOMO2D, the target V_P model and the seafloor-type geometry. Shot gathers shown in (c) and (d) are the same plotted in (a) and (b) respectively.

only the shallowest area up to ~ 0.75 km depth below the seafloor is well covered. The experiment geometry provides a total of 4,500 first arrival picks (plotted as blue dots in Fig. 3).

A series of inversion parameters have been tested, but only the ones providing the best result in terms of accuracy are shown in Table I. This table presents also the V_P model parameterization. As it usually occurs with geophysical inverse methods, the system to be inverted is underdetermined, meaning that the number of unknowns ($> 180,000$ nodes) is much larger than the number of equations (4,500 rays/travel times). Besides, ray paths with similar dips correspond to linearly dependent equations so that they do not allow to uniquely resolve the involved parameters. Therefore, regularization constraints should be introduced to reduce the number of independent variables and stabilize the inversion.

The initial model is a laterally homogeneous model with a vertical V_P gradient that follows the function $V_P(z) = 1.5 + 0.85 \cdot z$ (km/s), going from 1.5 km/s at the seafloor to 3.2 km/s at the maximum depth, Fig. 5a. This gradient differs substantially from the target one, so that we can consider that

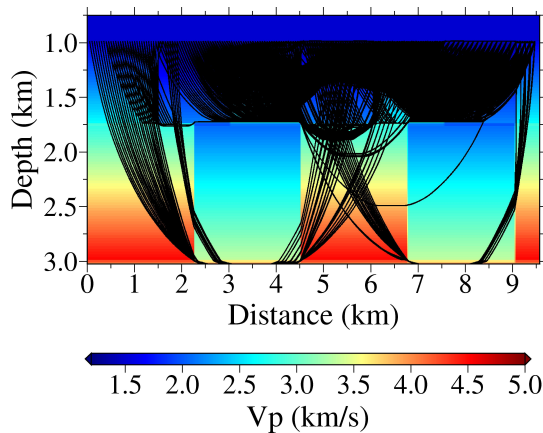


Fig. 4. First arrival ray paths for all the source-receiver pairs of the experiment with the seafloor-type geometry. Ray coverage indicates the areas where we have V_P information on the first arrival travel times. The model will be better resolved in the well-covered areas than in the poorly covered ones. The shallow part up to 0.75 km depth will be well constrained with this acquisition parameters and V_P model.

it does not contain a priori information. As is shown in Fig. 5b, the inverted V_P distribution follows the overall trends of the target V_P model (Fig. 5c), although it does not reproduce the sharp geometry and the correct amplitude of the anomalies. The differences between the initial (Fig. 5a), target (Fig. 5c), and the inverted (Fig. 5b) models are shown in Fig. 5d, 5e, and 5f, respectively. The maximum V_P difference in the shallowest part and the deeper central parts of the model are around ± 0.2 km/s (Fig. 5f). As expected, the larger differences concentrate in the sharp V_P contrasts, and in the poorly covered areas, especially in the deepest parts and in both edges of the model. Despite the different issues, the low-wavenumber information (i.e., the background gradient) in the shallow part of the model is successfully recovered after the TTT inversion.

In Fig. 6 we display the first arrival travel-time residuals as a function of source-receiver distance positions for the first (a) and last (b) iterations. Residual travel times are larger for the longer offsets because they correspond to the longest rays that accumulate more travel-time error and because those rays reach the deeper levels, where the V_P uncertainty is also larger. Initial residuals are negative on average because average V_P gradient in the initial model is weaker than in the target model so that V_P is lower. Residuals larger than 0.4 s caused by the central deep high- V_P anomaly are reduced to less than 0.1 s after the inversion. The largest residuals coincide with the location of the largest differences between initial and target model (Fig. 5d) and between the inverted and target models (Fig. 5f). The histogram in Fig. 7 shows the distribution of travel-time residuals for the first and last iterations. The mean and the standard deviation of the corresponding distributions diminishes from -142 ms and 143 ms (red columns) to a -0.8 ms and 30 ms (blue columns), respectively. The overall root mean square (RMS) travel-time residual is reduced from ~ 0.2 s in the first iteration to ~ 0.03 s in the final one, reflecting the improvement of the V_P model and the corresponding travel-time fitting after the inversion.

Fig. 8 shows the wavefields simulated using a finite dif-

ference acoustic solver [18], the seafloor-type geometry, and the initial, inverted, and target models, respectively. The comparison between the different wavefields clearly shows the improved first arrival fitting in the data domain. The wavefield simulated with the TTT inverted model (Fig. 8b) shows many of the seismic phases of the target wavefield (Fig. 8c), in contrast to what it is observed in the wavefield generated with the initial gradient model (Fig. 8a). A time shift of up to 0.3 s at 5 km offset distance between the first arrivals in Fig. 8a, and 8c is observed, whereas between Fig. 8b, and 8c it is of only 0.1 s. Aside from wave amplitudes, the main difference between the data generated with the inverted and target models are the reflected waves generated at the sharp boundaries between the different blocks, because only smooth gradients (i.e. low wavenumbers) can be recovered using first arrivals. The key observation is that the initial and target traces are cycle-skipped for the early arrivals (Fig. 8a, and 8c), whereas the inverted and target ones are not (Fig. 8b and 8c). At the farthest offset the inverted (Fig. 8b) and target (Fig. 8c) traces are starting to show some phase shift. However, the fact that the data are cycle-skipped for the gradient-based wavefield but not for most of the TTT inverted wavefield is key to justify their appropriateness to be used as initial model for FWI.

C. Full-Waveform Inversion

In this section we apply FWI to the original MCS data (Fig. 2b) using two different initial models. One is the linear vertical V_P gradient model already used as initial model to perform TTT (Fig. 5a) and the other is the V_P model obtained from TTT of DC first arrivals (Fig. 5b).

To perform the FWI we use the code presented in [30], and we analyze the possible issues that can drive the inversion into local minima. In subsection 1) we disentangle the instantaneous envelope and phase from the waveform to quantify the corresponding misfits between initial and target data. This helps in the design of a suitable objective function to mitigate the effects caused by the non-linearity. In 2) we analyse the cycle-skipping content depending on the initial model and inversion frequency. In 3) and 4) we show the FWI results.

1) *Prior study to FWI - Choosing a suitable objective function:* The seismic signal can be expressed as

$$u(t) = Env(t) \cdot \sin\theta(t) \quad (1)$$

where the envelope, $Env(t)$, and phase, $\theta(t)$, parameters are the instantaneous attributes of the wave [10], [20], [30], [31], [45], [46].

Under realistic conditions, phase and envelope differences between initial and target data can be large, and therefore the mixing between both parameters highly increases the non-linearity on top of the already existing one in FWI. In such cases, to decide the best parameterization to perform FWI, it is convenient to understand the characteristics of our data by disentangling first the phase and the envelope from each trace and quantifying the corresponding misfits between initial and target data.

In FWI, the alignment of the phases with the iterations is the most important task to diminish the cycle-skipping. If

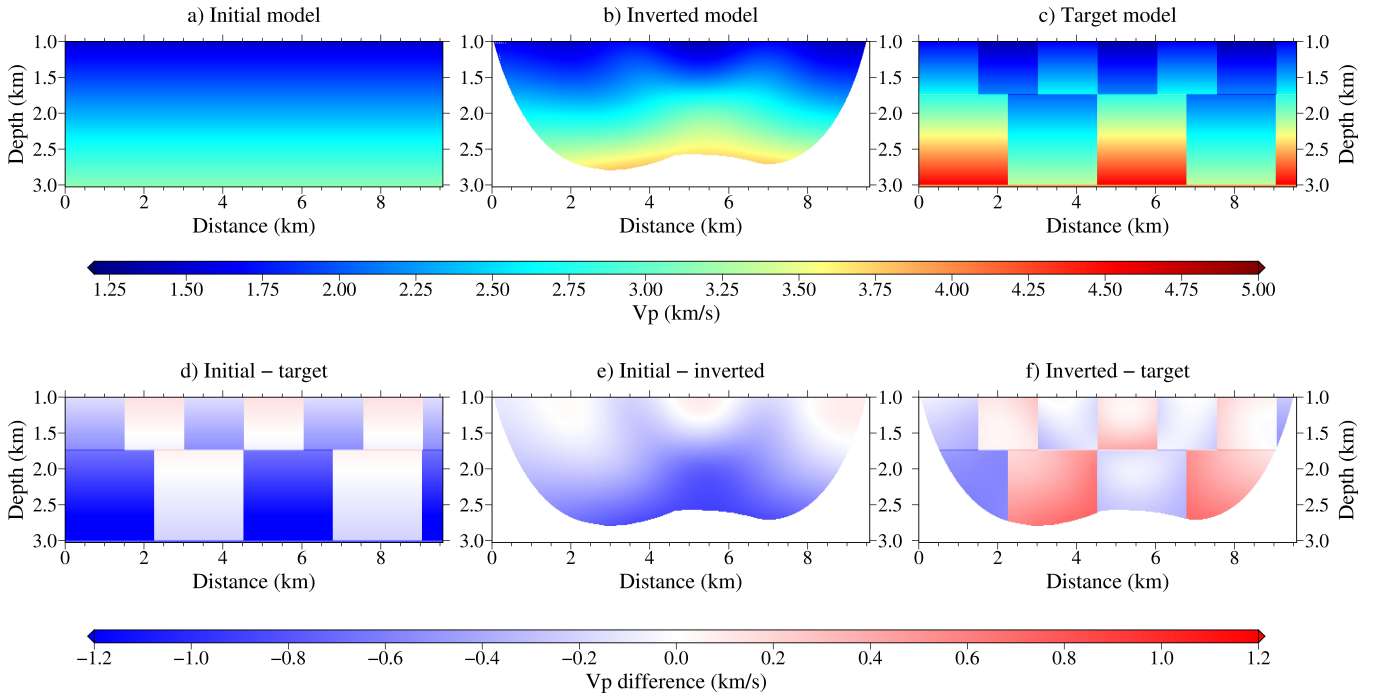


Fig. 5. 2-D Vp models for the TTT method. Uncovered areas (Derivative Weight Sum (DWS)=0, Toomey et al., 1994) are masked. (a) Initial Vp model, characterized by a laterally homogeneous model with a vertical Vp gradient. (b) Inverted Vp model obtained by TTT using the first arrivals of the DC MCS data (Fig. 3). (c) Target or checkerboard Vp model (Fig. 2a). Vp difference between: (d) initial and target model, (e) initial and inverted result, and (f) inverted result and target model.

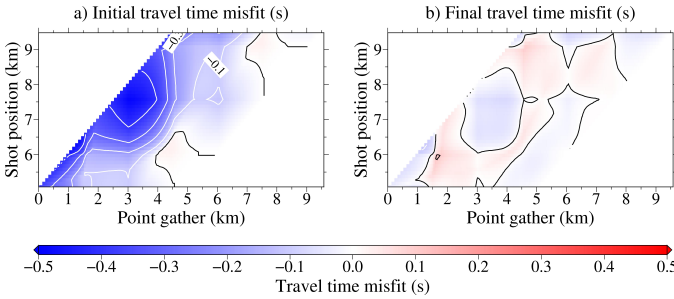


Fig. 6. Travel-time misfits after the first (a) and final (b) inversion step for each source-receiver pair along the profile. The colour scale shows misfit and the contour interval is 0.1 s.

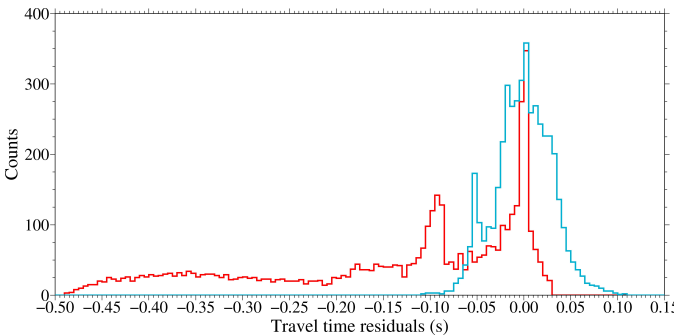


Fig. 7. Histogram of travel-time residuals obtained with the initial (red) and final (blue) models.

the envelope misfit is large, a phase-based objective function would show a more linear behavior than the original signal, and therefore a more suitable choice to perform FWI. In this

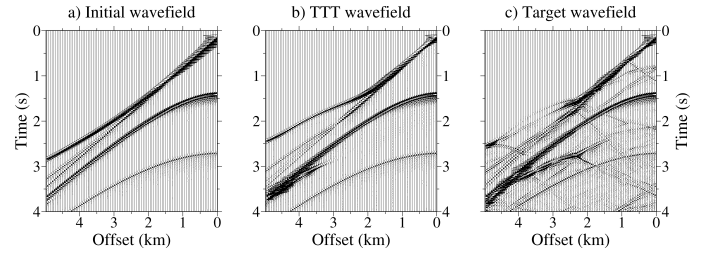


Fig. 8. Virtual downward continued wavefields generated using the FD solver (Dagnino et al., 2014) and the initial gradient (a), TTT inverted (b), and target (c) models in Figs. 5a, 5b, and 2a respectively. The source and receiver horizontal positions are the same as in Fig. 2. The two clear reflection events correspond to the reflection and multiple produced at the sea surface.

respect, it is crucial to use a continuous phase-based parameter which does not introduce numerical problems. An example of a convenient design for the instantaneous phase in the context of FWI is the normalized signal, $S_n = \sin(\theta)$ [31]. In [31], the normalized signal is used as inversion parameter due to the large envelope misfit between initial and target model. This choice diminishes the non-linearity and despite the presence of cycle-skipping, it is possible to invert a realistic target model with data lacking low frequencies and with no a priori information. However, in the present study, the envelope misfit is small in most of the events and this allows to directly use the signal as inversion parameter. This simplifies the methodology as no extra calculations are needed. We show in Fig. 9 the results of the misfits between the initial models and the target data (gradient, on the left column, and TTT, on the right column) for the signal (a and b), the envelope (c and d), and the normalized signal (e and f). The corresponding expressions

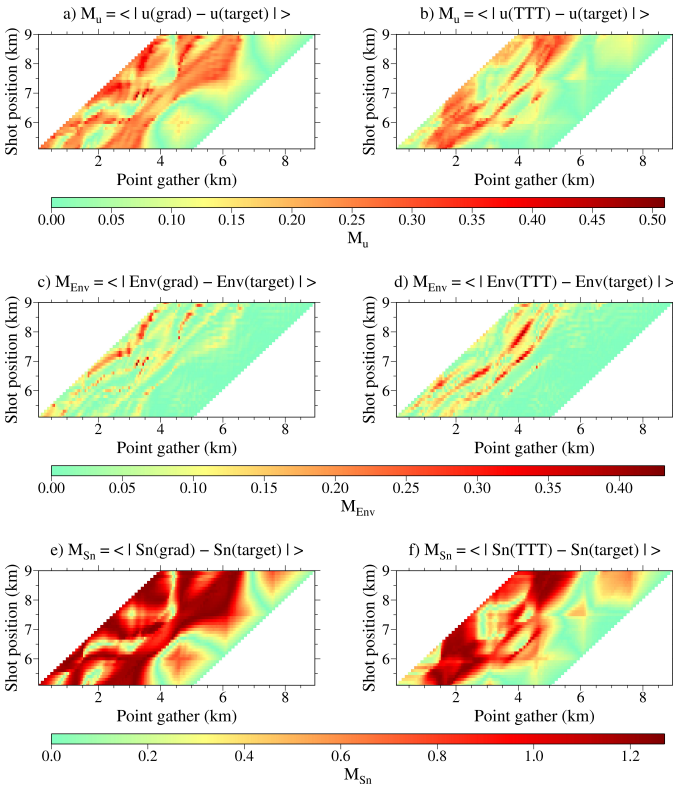


Fig. 9. Results of the misfits, M , between the initial models, gradient (left panels) and TTT model (right panels), and the target data filtered between 4 Hz and 4.5 Hz, for the signal (a and b), the envelope (c and d), and the normalized signal (e and f). At each panel, the x and y-axis refer to the position (km) of each point gather and shot gather along the model, respectively.

for the misfits are:

$$\langle M_u \rangle = \langle |u(\text{init}) - u(\text{target})| \rangle \quad (2)$$

$$\langle M_{Env} \rangle = \langle |Env(\text{init}) - Env(\text{target})| \rangle \quad (3)$$

$$\langle M_{Sn} \rangle = \langle |Sn(\text{init}) - Sn(\text{target})| \rangle \quad (4)$$

For these calculations, the data is filtered between 4 Hz and 4.5 Hz as 4 Hz is a realistic value for the lowest frequency available in field data. The three misfits are averaged in a 20% of the shot gather, i.e. within a time window of 1.6 seconds from the first arrival. We limit the time window to the early arrivals because it is the most important area to fit first. To do this, the traces at each receiver are normalized to 1. Fig. 9 shows, for both initial models, the well fitted envelope misfit and how the Sn misfit features reflects in the general aspect of the signal misfit. These results, as already mentioned above, confirm the usage of the signal as inversion parameter for both initial models, as the non-linear effects coming from the amplitude differences are negligible. We refer to the Supplementary material (S2) for more specific details.

In summary, in this study we use as objective function the L2-norm of the waveforms. The minimization is done applying the non-linear conjugate gradient method as search direction algorithm.

2) *Prior study to FWI - Study of the cycle-skipping with the initial model and frequency content in the data set:* To understand and quantify the frequency gap for both initial models, we perform several tests using data without low frequencies. The data low-pass filtered at different cutoffs (from 1 Hz to 6 Hz) is shown in the Supplementary material (S3). To assess the validity of the initial V_P models in a systematic manner, we estimate the amount of cycle skipping between target and initial traces calculating the first arrival phase misfit ($\Delta\theta$) in time domain as:

$$\Delta\theta_{ij} = 2 \cdot \pi \cdot v \cdot [FA_{ij}(\text{initial}) - FA_{ij}(\text{target})] \quad (5)$$

where v [Hz] is the frequency at which the data is filtered (bandpass between $[v, v+0.5]$ Hz) and the first arrival travel time is denoted by FA_{ij} [s], where the indexes i and j refer to the shot and receiver position, respectively. We limit the cycle skipping study at first arrivals (using the DC data) because its optimal fitting at the first iterations of the inversion is the key to achieve proper inversion results. Fig. 10 shows the phase misfit ($\Delta\theta_{ij}/\pi$) for the two initial models and different frequency cutoffs, from 1Hz to 6 Hz. Whenever the absolute value of $|\Delta\theta_{ij}/\pi|$ is greater than 1, $|\Delta\theta_{ij}/\pi| > 1$, it is considered that there is cycle skipping between the two traces, and the corresponding points are shown in black color in the figure. A frequency gap is implicit in the areas where we observe cycle skipping. As the frequency-cutoff of the data (i.e. initial FWI frequency) increases, the value of the $\Delta\theta_{ij}/\pi$ misfit generally increases too, and new areas with cycle-skipped traces appear. Additionally, the figure shows significant differences between the two initial models. The TTT-inverted result (b) is a better-posed initial model than the gradient model one (a) regardless of the starting frequency. It is also noticeable the difference in the spatial distribution of cycle-skipped traces. In the gradient model, the traces out of phase are grouped together in the same areas of the model, which will be hardly recovered in the inversion process. However, in the TTT model the conflicting areas can be more easily inverted as cycle-skipped traces are less concentrated in particular locations.

Fig. 11 is an overview of Fig. 10, which shows the information of the different panels summarized in one panel for each initial model. It shows the percentage of traces (y-axis) within a certain range of $\Delta\theta_{ij}/\pi$ misfit values at each frequency (x-axis). The distribution for the cycle-skipped traces is also shown. At 1 Hz, 65% of traces are in phase (circles) for the gradient model and 100% for the TTT model, so there is no cycle-skipping at all (crosses). When the cut-off frequency increases, the number of aligned traces (circles) decreases, whereas the number of cycle-skipped traces (crosses) increases. At 6 Hz, the gradient model data has $\sim 50\%$ of the traces cycle-skipped, whereas for the TTT initial model they do not exceed $\sim 35\%$. The features described from Fig. 10 and Fig. 11 favors the TTT model over the linear gradient to be used as initial model for FWI for all the starting frequencies tested.

Data with $\Delta\theta_{ij}/\pi$ misfits between 0.25 and 0.5 (squares) represent a 20% of all traces at practically all frequencies.

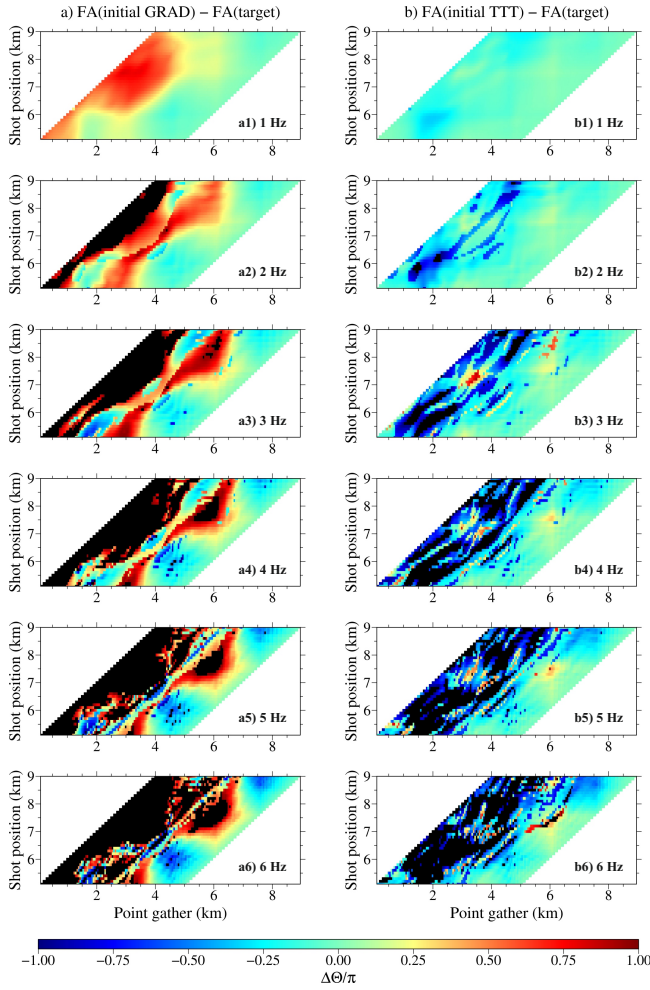


Fig. 10. Cycle skipping study for all the shots (y-axis) and point gathers (x-axis) along the model. The $\Delta\theta_{ij}/\pi$ misfit is calculated for the initial-target data and different frequency cutoffs 1) 1 Hz, 2) 2 Hz, 3) 3 Hz, 4) 4 Hz, 5) 5 Hz and 6) 6 Hz. (a) Left panels correspond to the linear Vp-gradient initial model and (b) right panels to the TTT inverted result. Green areas are in phase, while dark red and blue areas show the highest $\Delta\theta_{ij}/\pi$ misfits. The black areas point at the cycle skipped traces.

The same happens for $\Delta\theta_{ij}/\pi$ misfits between 0.5 and 1 (triangles), except for the highest frequencies (5 - 6 Hz). In this case, these traces with large $\Delta\theta_{ij}/\pi$ values are now cycle-skipped (crosses). In summary, the cycle skipping tests in Fig. 11 indicate the quality and potential of the initial models and predicts their expected performance in FWI.

3) *FWI results using the V_P -gradient as initial model:* A total of 45 shot gathers (4,500 seismograms) with no preprocessing are used as input data set for the inversion (see Fig. 2b). We apply a conventional multi-scaling strategy [15] that consists on including progressively higher-frequencies in the input data in order to incorporate higher-wavenumber details of the model at each FWI step. A band-pass Butterworth filter is applied to the inverted data set prior to the inversion. We consider that there is no signal above noise level below the lowest inverted frequency. A maximum of 20 iterations are performed per frequency band. At each step of the inversion, we increase the inverted frequency band by 0.5 Hz up to the

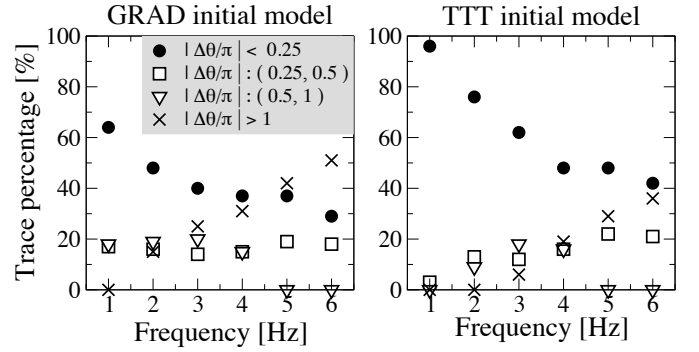


Fig. 11. General cycle skipping study at different initial inversion frequencies. The $\Delta\theta_{ij}/\pi$ misfit is calculated and sorted in four intervals (symbols: circle $|\Delta\theta_{ij}/\pi| < 0.25$; square $0.25 < |\Delta\theta_{ij}/\pi| < 0.5$; triangle $0.5 < |\Delta\theta_{ij}/\pi| < 1$, and cross $|\Delta\theta_{ij}/\pi| > 1$, cycle skipped traces). Each symbol is plotted for each frequency (x-axis) every 1 Hz, from 1 Hz up to 6 Hz, and the corresponding percentage value of traces (y-axis) in the data with that amount of $\Delta\theta_{ij}/\pi$ misfit. Left panel refers to the Vp-gradient initial model, and right panel refers to the TTT model.

final inverted frequency of 9.5 Hz. We start by showing the inversion result from 1 Hz for reference, and progressively display their evolution and deterioration from an ideal situation to the real or worst case scenario (3 Hz). The size of the space grid is 12.5 m, so that we have a total of 768 x 244 nodes.

In this section, we perform FWI using the linear V_P -gradient, i.e. same initial model as for TTT (see Fig. 5a). The first column (a) in Fig. 12 shows the V_P models obtained after the FWI starting at (1) 1 Hz, (2) 2 Hz, and (3) 3 Hz, respectively. The second column (b) is the V_P difference between inverted results shown in (a) and the target model (Fig. 2a). Finally, the third column (c) shows $\Delta\theta_{ij}/\pi$ for the models obtained by FWI shown in (a).

When the starting frequency is 1 Hz, the target model is well recovered (Fig. 12(a1)). Differences concentrate at the left hand side and lower right corner (Fig. 12(b1)) where there is low data coverage. $\Delta\theta_{ij}/\pi$ misfit values in panel (c1) are low due to the good match between target and most of the (a1) model.

When the inversion starts at 2 Hz, half of the model is not well recovered (panels (a2) and (b2)). The upper central and right anomalies are well-retrieved, but the inversion fails reconstructing the lower central anomaly and the left hand side of the model. That is because the deeper and left areas are covered by few traces that are initially cycle-skipped (Fig. 10(a2)). Panel (c2) shows that traces at near offsets are still in phase. However, cycle-skipping arise for far offsets (left hand side in the panel c2) and the inversion fails at recovering this part of the model. The low-velocity anomalies on the left hand side are better retrieved than the ones with high-velocities because the V_P -gradient is close to the initial one (Fig. 5d).

Finally, when the initial inversion frequency is 3 Hz, the inversion fails (panel a3). During the inversion, only the shallowest central anomaly at 4.5 - 6 km offset distance is -very roughly- recovered. The boundaries and the internal gradient cannot be reconstructed. The other parts of the model remain unaltered. Thus, the model in (a3) is very similar to the initial model (Fig. 5a), the V_P difference in (b3) to Fig.

5d, and the $\Delta\theta_{ij}/\pi$ misfit in (c3) to Fig. 10(a3). As expected, when the initial model is poor the inversion fails when the inversion starts at realistic frequencies.

4) *FWI results using the model inverted by TTT as initial model:* We repeated the analysis in the previous section but using the model obtained by TTT (Fig. 5b) as initial model instead of the V_P -gradient one. As in Fig. 12, the first column (a) in Fig. 13 shows the V_P models obtained after the FWI, but this time starting at (1) 1 Hz, (2) 2 Hz, (3) 3 Hz, (4) 4 Hz, (5) 5 Hz, and (6) 6 Hz, respectively. The second column (b) is the V_P difference between results in (a) and the target model (Fig. 2a), and third column (c) $\Delta\theta_{ij}/\pi$ for the model in (a) and the target ones.

Panels (a1), (a2), (a3), and (a4) display models that match the target one (Fig. 2a). Their differences are negligible in almost the entire model, except for the left corner (Fig. 13(b1), (b2), (b3), and (b4)) where the data coverage is poor. Only few traces at far offsets illuminate the left hand side of the model, so the large discrepancies are not reduced. Those point gathers correspond to the traces located at the end of the streamer. The spots of cycle skipping in panels (c3), and (c4) are caused by the point gathers located below ~ 1 km at the model. The successful inversion when using the TTT result as initial model is reflected in the improvement of the cycle-skipping in panels (c1), (c2), (c3), and (c4), whose value is almost 0 in most of the panels. Their $\Delta\theta_{ij}/\pi$ misfits have greatly reduced as compared with the initial ones (panels (b3), and specially (b4) in Fig. 10) with multiple patches of cycle skipping.

On the other hand, panels (a5) and (a6) show several V_P -artifacts on the left and lower anomalies. In addition, the boundaries of the lower anomalies are not completely vertical. Thus, V_P -differences concentrate in these regions (Fig. 13(b5) and (b6)). Panels (c5) and (c6) confirm that the FWI results (Fig. 13(a5), and (a6)) differ from the target one (Fig. 2a), because they have multiple areas where the $\Delta\theta_{ij}/\pi$ misfit is significant, with even some cycle skipping. The errors coincide with the largest model differences (Fig. 13(b5), and (b6)), and it is caused by the lack of low frequency information on the data and lack of illumination or ray coverage. Finally, Fig. 13 shows that to successfully invert data when low frequencies are not available (below 4 Hz) requires an adequate initial model such as the one provided by TTT.

A detailed analysis of the FWI results of data lacking frequencies below 4 Hz and using the TTT inverted model as initial one is shown in the Supplementary material (S4). The V_P models obtained after several multi-scaling steps of the FWI are shown in Fig. S03. In addition, the comparison of 1-D vertical V_P depth profiles for the initial (V_P -gradient and TTT), FWI result and target models, are shown in Fig. S04. Figs. S03 and S04 illustrate the high resolution of FWI models, which is better than the one obtained by TTT, as referred in the Introduction. Figs. S05 and S06, further illustrate the improvement of data fit throughout the inversion process. The analysis is done specifically for this case as it is the one providing the best results under realistic conditions (Fig. 13(a4), (b4), (c4)). Furthermore, we refer to the Supplementary material (S5) for details about a more realistic situation in which different noise levels are added to the data set (Fig.

S07) prior to FWI. All the results (Fig. S08) match with Fig. 13(a-b)4. These results indicate that the FWI results are robust under realistic noise conditions if a good initial model, such as that provided by TTT of DC streamer data, is used, and the workflow proposed in this paper is followed.

IV. DISCUSSION

We present a workflow composed on three main steps; DC, TTT and FWI, to obtain high resolution complex models of the subsurface including V_P inversions and vertical boundaries with abrupt V_P contrasts. We show that if the workflow is followed, FWI can be successfully applied to field seismic data sets collected under realistic experimental conditions. The workflow reveals the low-wavenumber information hidden in the band-limited data to obtain an initial model for FWI. Although ad hoc methodologies may benefit particular experimental seismic settings to obtain a successful FWI (e.g. [19], [55]), our workflow provides a generalist procedure that can potentially be applied to most existing data sets. The workflow explains the necessary steps to identify cycle-skipped phases, exclude them from the inversion if necessary to mitigate the non-linearity during FWI, and presents the methodology to design a suitable objective function depending on the characteristics of the input data.

The first step is the DC method, which eliminates the effect of the water column to identify the early refractions containing the low-wavenumber information in their travel times (e.g. [17], [34]). Applying DC to change the geometry set up from the sea level to the seafloor surface promotes the appearance of refracted phases as first arrivals [26] along the whole offset range [22] for most experiments. Comparing the virtual shot gathers after the DC of the simulated data, with the record from the virtual acquisition geometry (Fig. 3) shows that the DC method works well because most phases occur in both records at the same two way travel time. However, first arrivals are not always easy to track, for example at near offsets the energy collapses to an area wider than a point. Also, when first arrivals at far offsets are affected by attenuation effects, they appear less focused due to the finite nature of the seismic record used as equivalent source, (Fig. 3a). Moreover, it also produces upward diffraction tails. The discrete nature of the input wavefield recordings may produce aliasing effects in the final DC data depending of sources and/or receivers spacing.

The synthetic data show that DC first arrivals match well the simulated arrivals from forward modelling techniques (wave equation solvers and TOMO2D) for nearly all offsets (Fig. 3a). Therefore, these phases contain correct subsurface V_P information. While first arrival travel times are correctly retrieved, wave amplitudes are however not well-preserved [50]. Hence, for the next step we use TTT with first arrival travel times of DC shot gathers.

Unlike previous synthetic studies combining TTT and FWI that use both sources and receivers fixed and placed all along the model (e.g. [2], [3], [8]), our approach is a more realistic geometry of a marine experiment facing the problems of limited coverage and illumination. The main issue to perform TTT is the identification of refractions as first arrivals, especially

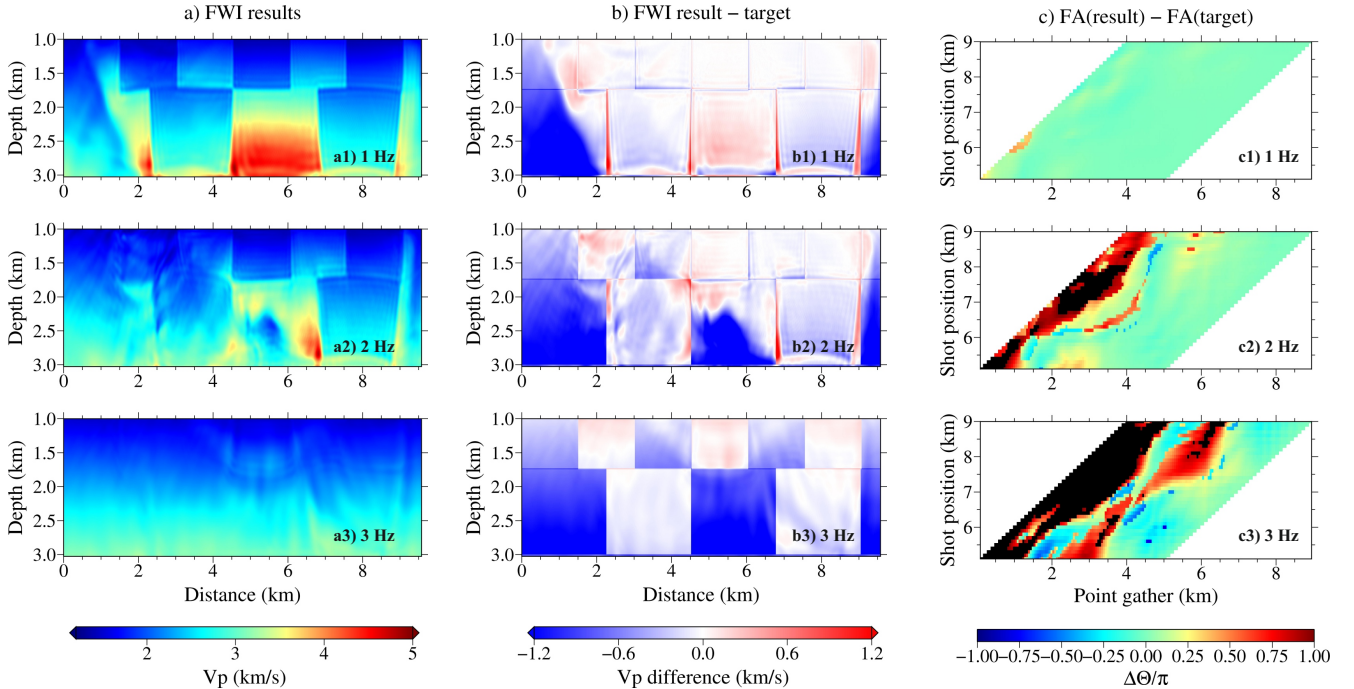


Fig. 12. (a) FWI results retrieved after the multi-scaling strategy starting at 1) 1 Hz, 2) 2 Hz, and 3) 3 Hz, respectively; and using the linear V_P -gradient as initial model. (b) V_P difference between FWI results in (a) and the target model (Fig. 2a). (c) $\Delta\theta_{ij}/\pi$ misfit calculated for the FWI results in (a) for all the shots (y-axis) and point gathers (x-axis) along the model depending on the initial inversion frequency, 1) 1 Hz, 2) 2 Hz, and 3) 3 Hz, respectively.

in ≤ 9 km offset and deep water. Given a positive V_P -depth gradient, the steepness of the V_P gradient and source-receiver distance are key to determine the maximum depth reached by turning rays (Fig. 1). Early refraction travel times in the inversions provide a better-constrained upper part of the model (Fig. 5b) [4], instead of being conditioned by the smoothness regularization constraints, that help to properly retrieve not only the shallow but also the deep areas. Thus, applying DC to the seafloor is necessary to recover these first arrivals phases in the shot gathers [26] all over the offset range (Fig. 3).

TTT models from DC first arrivals have the largest travel-time residuals or V_P differences in the areas with strong V_P contrasts (Fig. 5). To successfully map large V_P contrasts, reflections from the discontinuity must be jointly inverted. Of course poor ray coverage (low DWS) also cause poor V_P retrieval at the edges and deeper parts of the model (see Fig. 5f). Besides, the low resolution observed at depth is also related to the small wavenumbers of the deep anomalies.

The reduction of the travel-time residuals between initial and final TTT models is significant in the data domain (Fig. 7) for all offsets (see Fig. 6), in agreement with V_P model results (see Figs. 5d-f). The wavefield simulated using the TTT model is closer to the target wavefield than data generated with the assumed gradient model (see Fig. 8). Major differences concentrate in reflected phases, where V_P changes abruptly. Initial and target first arrivals display larger time shifts as offset increases (at > 2 km offset, being up to 0.3 s at 5 km offset distance, see Fig. 8).

A key point is that most seismic traces modeled using

the TTT V_P are not cycle-skipped with respect to the target traces. In contrast, the results obtained using a gradient-based model display cycle skipping even at the lowest frequencies (see Figs. 10, 11). We estimate the frequency gap indirectly by computing the cycle skipping between initial V_P model and the data content for FWI in Figs. 10, and 11. In particular, these figures allow to assess the frequency gap between the shortest wavelength retrieved in TTT and the largest one in FWI. Minimizing this gap and, therefore the cycle skipping between initial and target data, is essential for FWI (see Fig. 10 versus Figs. 12, 13) to retrieve accurate V_P , avoid artifacts (see Figs. 12(a-b-c)2, 13(a-b-c)5-6) and prevent the inversion to get stuck in local minima (Figs. 12(a-b-c)3).

We verified that the model is kinematically correct (not cycle-skipped), by comparing the $\Delta\theta_{ij}/\pi$ differences in DC data (Figs. 10, 11), since low-wavenumber information of the media is shown in the first arrivals. Nonetheless, recovery of V_P inversions and vertical V_P contrasts, such as the edges of the checkerboard model anomalies, is incomplete with TTT and normally requires applying FWI.

FWI is the final workflow step and requires a robust initial V_P model to avoid cycle skipping (e.g. [12], [14], [39], [40], [52]). When this condition is fulfilled, our synthetic test shows that FWI allows fitting most seismic events (Fig. S05) providing a higher-resolution V_P model (Fig. 13(a-b-c)4). It has been shown that TTT models from ultra-long offset streamers (e.g. [47], [51]) and, TTT models obtained from DC first arrivals (Figs. 3c, 5b) are robust to perform FWI (Figs.

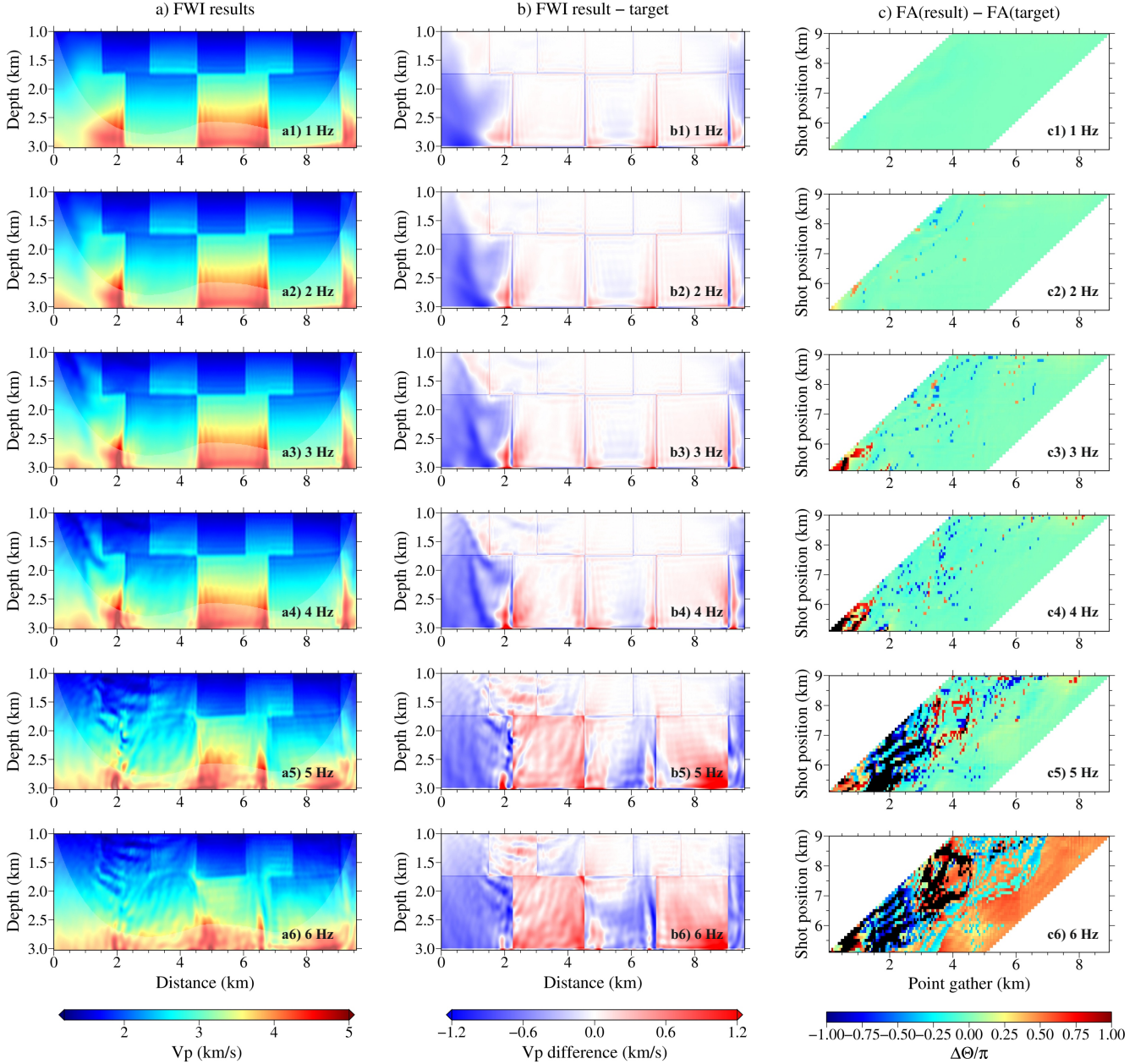


Fig. 13. (a) FWI results retrieved after the multi-scaling strategy starting at 1) 1 Hz, 2) 2 Hz, 3) 3 Hz, 4) 4 Hz, 5) 5 Hz, and 6) 6 Hz, respectively; and using the TTT inverted result as initial model. Uncovered areas (DWS=0) are lighter to better see the regions where low-frequency information is recovered by the TTT. (b) Vp difference between FWI results in (a) and the target model (Fig. 2a). (c) $\Delta\theta_{i,j}/\pi$ misfit calculated for the FWI results in (a) depending on the initial inversion frequency, 1) 1 Hz, 2) 2 Hz, 3) 3 Hz, 4) 4 Hz, 5) 5 Hz, and 6) 6 Hz, respectively.

10, 11, 13). In our synthetic tests, most differences between the FWI and target models occur where the initial TTT model is poorly constrained due to limited data coverage (see Figs. 5f, 13).

The wavefield generated using the final FWI model (Fig. S05b) and its corresponding target seismic record (Fig. S05c) match for all offsets and times (Fig. S05e) when initial model is from TTT (Figs. 10, 11). In this case, FWI is capable of decreasing the wavefield misfit close to zero (Figs. S05e, S06).

The workflow provides robust FWI results even when input data lowest frequencies are 4-5 Hz, as for most marine surveys.

Our workflow will work regardless of the V_P distribution of the medium. That is, the workflow is equally valid if the medium is smooth without reflections (in this case the refraction (DC) TTT will be key to define the background), or if it has numerous reflections or few but separate ones, which according to their dimensions will be recovered with either TTT and/or FWI. Our synthetic results show that using

our workflow even vertical V_P boundaries and V_P inversions, similar to those expected across steep faults or salt diapirs (in [9], [11], [41]), can be properly mapped with limited-offset data sets, but the maximum target depth to be resolved has to be evaluated from the V_P structure and experiment design (Figs. 1, 4).

mds

September 24, 2020

V. CONCLUSION

We present a practical appraisal for waveform tomography of band- and offset-limited streamer seismic data. We show that high-quality V_P models of complex structures can be obtained using traditional marine data sets, archives at many organizations, provided the appropriate workflow is applied. We provide the sequence of steps, DC of the MCS data to the seafloor, TTT of DC first arrivals, and FWI of the original MCS data, to be followed to successfully retrieve a high resolution V_P model. We test results after each step, and show a study prior to and after the FWI at different and challenging experimental conditions. For this reason, we test the FWI with the two most widely used initial V_P models (linear gradient and TTT result) and a range of data frequency content from 1 up to 6 Hz. We show in both a visual and quantitative way for each case the areas that suffer from cycle skipping problems. We also show how the TTT result of DC first arrivals, within its resolution range, is a useful model to reduce the non-linearity of FWI. We test a complex synthetic model with vertical V_P boundaries and V_P inversions for assessment of the results. Our results indicate that much of the existing multichannel marine streamer data sets are suitable to obtain high resolution V_P information of the subsurface.

ACKNOWLEDGMENT

The authors would like to thank Matthias Delescluse and two anonymous reviewers whose comments/suggestions helped to improve and clarify this article. We also thank to Ramon Carbonell for his recommendation to publish this synthetic study. Part of this work is presented at the PhD thesis of [23] performed at the UB. This is a contribution of the Barcelona Center for Subsurface Imaging that is a Grup de Recerca 2017 SGR 1662 de la Generalitat de Catalunya. This work has been done in the framework of project FRAME (Reference CTM2015-71766-R) and project ATLANTIS PID2019-109559RB-I00, funded by the Spanish Ministry of Research and Innovation and has also had the funding support of the Severo Ochoa Centre of Excellence accreditation (CEX2019-000928-S), of the Spanish Research Agency (Agencia Española de Investigación, AEI). Generic Mapping Tools [56] was used in the preparation of this manuscript.

REFERENCES

- [1] S. Abreo, A. Ramirez, F. Vivas, H. Gonzalez, E. Wiarda, R. Martinez, J.O. Serrano and C. Gonzalez, "Diving-wave FWI methodology applied to a Colombian Caribbean data set", *The Leading Edge*, vol. 37, no. 4, pp. 291-295, Apr. 2018, <https://doi.org/10.1190/tle37040291.1>.
- [2] H.S. Aghamiry, A. Gholami and S. Operto, "Robust wavefield inversion via phase retrieval", *Geophys. J. Int.*, vol. 221, no. 2, pp. 1327-1340, May 2020a, <https://doi.org/10.1093/gji/ggaa035>.
- [3] H.S. Aghamiry, A. Gholami and S. Operto, "Full Waveform Inversion by Proximal Newton Method using Adaptive Regularization", *Geophys. J. Int.*, Accepted Manuscript, ggaa434, Sep. 2020b, <https://doi.org/10.1093/gji/ggaa434>.
- [4] A.F. Arnulf, A.J. Harding, G.M. Kent, S.C. Singh and W.C. Crawford, "Constraints on the shallow velocity structure of the Lucky Strike Volcano, Mid-Atlantic Ridge, from downward continued multichannel streamer data", *J. Geophys. Res. Solid Earth*, vol. 119, no. 2, pp. 1119-1144, Jan. 2014, <http://doi.org/10.1002/2013JB010500>.
- [5] S. Begović, A. Meléndez, C.R. Ranero and V. Sallarès, "Joint refraction and reflection travel-time tomography of multichannel and wide-angle seismic data", *EGU General Assembly*, Vienna, Austria, 23-28 April 2017, EGU2017-17231, 2017.
- [6] J.R. Berryhill, "Wave-equation datuming", *Geophysics*, vol. 44, no. 8, pp. 1329-1344, Aug. 1979, <https://doi.org/10.1190/1.1441010>.
- [7] J.R. Berryhill, "Wave-equation datuming before stack", *Geophysics*, vol. 49, no. 11, pp. 2064-2066, Nov. 1984, <https://doi.org/10.1190/1.1441620>.
- [8] B. Biondi and A. Almomin, "Tomographic full-waveform inversion (TFWI) by combining FWI and wave-equation migration velocity analysis", *The Leading Edge*, vol. 32, no. 9, pp. 1074-1080, Sep. 2013, <https://doi.org/10.1190/tle32091074.1>.
- [9] F. Bleibinhaus, J.A. Hole, T. Ryberg and G.S. Fuis, "Structure of the California Coast Ranges and San Andreas Fault at SAFOD from seismic waveform inversion and reflection imaging", *J. Geophys. Res.*, vol. 112, no. B6, B06315, Jun. 2007, <https://doi.org/10.1029/2006JB004611>.
- [10] E. Bozdağ, J. Trampert and J. Tromp, "Mist functions for full waveform inversion based on instantaneous phase and envelope measurements", *Geophys. J. Int.*, vol. 185, no. 2, pp. 845-870, May 2011, <https://doi.org/10.1111/j.1365-246X.2011.04970.x>.
- [11] S. Brandsberg-Dahl, N. Chemingui, A. Valenciano, J. Ramos-Martinez and L. Qiu, "FWI for model updates in large-contrast media", *The Leading Edge*, vol. 36, no. 1, pp. 81-87, Jan. 2017, <https://doi.org/10.1190/tle36010081.1>.
- [12] R. Brossier, S. Operto and J. Virieux, "Seismic imaging of complex onshore structures by 2D elastic frequency-domain full-waveform inversion", *Geophysics*, vol. 74, no. 6, pp. WCC105-WCC118, Nov. 2009, <https://doi.org/10.1190/1.3215771>.
- [13] R. Brossier, "Two-dimensional frequency-domain visco-elastic full waveform inversion: Parallel algorithms, optimization and performance", *Computers & Geosciences*, vol. 37, no. 4, pp. 444455, Apr. 2011, <https://doi.org/10.1016/j.cageo.2010.09.013>.
- [14] R. Brossier, S. Operto and J. Virieux, "Velocity model building from seismic reflection data by full-waveform inversion", *Geophysical Prospecting EAGE*, vol. 63, no. 2, pp. 354-367, 2015, <http://doi.org/10.1111/1365-2478.12190>.
- [15] C. Bunks, F.M. Saleck, S. Zaleski and G. Chavent, "Multiscale seismic waveform inversion", *Geophysics*, vol. 60, no. 5, pp. 1457-1473, Sep. 1995, <http://doi.org/10.1190/1.1443880>.
- [16] J.M. Carcione, G.C. Herman and A.P.E. ten Kroode, "Seismic modeling", *Geophysics*, vol. 67, no. 4, pp. 1304-1325, Jul. 2002, <https://doi.org/10.1190/1.1500393>.
- [17] Y. Cho, W. Ha, Y. Kim, S. Shin and E. Park, "Laplace-Fourier-Domain Full Waveform Inversion of Deep-Sea Seismic Data Acquired with Limited Offsets", *Pure Applied Geophysics*, vol. 173, pp. 749-773, March 2016, <http://doi.org/10.1007/s00024-015-1125-7>.
- [18] D. Dagnino, V. Sallarès and C.R. Ranero, "Scale- and parameter-adaptive model-based gradient pre-conditioner for elastic full-waveform inversion", *Geophys. J. Int.*, vol. 198, no. 2, pp. 1130-1142, Aug. 2014, <http://doi.org/10.1093/gji/ggu175>.
- [19] M. Delescluse, M.R. Nedimović and K.E. Loudon, "2D waveform tomography applied to long-streamer MCS data from the Scotian Slope", *Geophysics*, vol. 76, no. 4, pp. B151B163, Jul. 2011, <https://doi.org/10.1190/1.3587219>.
- [20] A. Fichtner, B.L.N. Kennett, H. Igel and H.-P. Bunge, "Theoretical background for continental- and global-scale full-waveform inversion in the timefrequency domain", *Geophys. J. Int.*, vol. 175, no. 2, pp. 665685, Nov. 2008, <https://doi.org/10.1111/j.1365-246X.2008.03923.x>.
- [21] D. Ghosal, S.C. Singh and J. Martin, "Shallow subsurface morphotectonics of the NW Sumatra subduction system using an integrated seismic imaging technique", *Geophys. J. Int.*, vol. 198, no. 3, pp. 1818-1831, Sep. 2014, <https://doi.org/10.1093/gji/ggu182>.
- [22] C. Gras, D. Dagnino, C.E. Jiménez-Tejero, A. Meléndez, V. Sallarès and C.R. Ranero, "Full waveform inversion of short-offset, band-limited

- seismic data in the Alboran basin (SE Iberia)", *Solid Earth*, vol. 10, no. 6, pp. 18331855, . 2019, <https://doi.org/10.5194/se-10-1833-2019>.
- [23] C. Gras, "Inversion of multichannel seismic data by combination of travel-time and full waveform tomography", *Ph.D. dissertations*, University of Barcelona, Barcelona, Spain, 2019, URI: <http://hdl.handle.net/2445/149360>.
- [24] I. Grevemeyer, C.R. Ranero and M. Vandic, "Structure of oceanic crust and serpentinitization at subduction trenches", *Geosphere*, vol. 14, no. 2, pp. 395418, Jan. 2018, <https://doi.org/10.1130/GES01537.1>.
- [25] A.S. Henig, D.K. Blackman, A.J. Harding, J.P. Canales and G.M. Kent, "Downward continued multichannel seismic refraction analysis of Atlantis massif oceanic core complex, 30N, mid-Atlantic ridge", *Geochem. Geophys. Geosy.*, vol. 13, no. 5, Q0AG07, May 2012, <https://doi.org/10.1029/2012GC004059>.
- [26] A.S. Henig, "Seismic structure of shallow lithosphere at locations of distinctive seafloor spreading", Ph.D. dissertations, University of California San Diego, ProQuest ID: Henig_ucsd_0033D_13084, Merritt ID: <ark:/20775/bb0240289d>, 2013, Retrieved from <https://escholarship.org/uc/item/7rz620vz>.
- [27] J.W.D. Hobro, S.C. Singh and T.A. Minshall, "Three-dimensional tomographic inversion of combined reflection and refraction seismic traveltime data", *Geophys. J. Int.*, vol. 152, no. 1, pp. 79-93, Jan. 2003, <https://doi.org/10.1046/j.1365-246X.2003.01822.x>.
- [28] J.A. Hole, R.D. Catchings, K.C.St. Clair, M.J. Rymer, D.A. Okaya and B.J. Carney, "Steep-Dip Seismic Imaging of the Shallow San Andreas Fault Near Parkfield", *Science*, vol. 294, no. 5546, pp. 1513-1515, Nov. 2001, <https://doi.org/10.1126/science.1065100>.
- [29] W. Hu, J. Chen, J. Liu and A. Abubakar, "Retrieving Low Wavenumber Information in FWI: An Overview of the Cycle-Skipping Phenomenon and Solutions", *IEEE Signal Processing Magazine*, vol. 35, no. 2, pp. 132-141, Mar. 2018, <https://doi.org/10.1109/MSP.2017.2779165>.
- [30] C.E. Jiménez Tejero, D. Dagnino, V. Sallarès and R.C. Ranero, "Comparative study of objective functions to overcome noise and band-width limitations in full waveform inversion", *Geophysical J. Int.*, vol. 203, no. 1, pp. 632-645, Oct. 2015, <http://doi.org/10.1093/gji/ggv288>.
- [31] C.E. Jiménez-Tejero, V. Sallarès and C.R. Ranero, "Appraisal of Instantaneous Phase-Based Functions in Adjoint Waveform Inversion", *IEEE Transactions on Geoscience and Remote Sensing*, vol. 56, no. 9, pp. 5185-5197, Sep. 2018, <https://doi.org/10.1109/TGRS.2018.2811245>.
- [32] J. Korenaga, W.S. Holbrook, G.M. Kent, P.B. Kelemen, R.S. Detrick, H.-C. Larsen, J.R. Hopper and T. Dahl-Jensen, "Crustal structure of the southeast Greenland margin from joint refraction and reflection seismic tomography", *J. Geophys. Res.*, vol. 105, no. B9, pp. 21591-21614, Sep. 2000, <https://doi.org/10.1029/2000JB900188>.
- [33] P. Lailly, "The seismic inverse problem as a sequence of before stack migrations: Conference on Inverse Scattering, Theory and Application", *Society for Industrial and Applied Mathematics*, in edited by J. Bednar et al., Expanded Abstracts, 206-220, SIAM, Philadelphia, Penn, 1983.
- [34] M. Marjanovic, R.-E. Plessix, A. Stopin and S. Singh, "Elastic versus acoustic 3-D Full Waveform Inversion at the East Pacific Rise 9°50'N", *Geophys. J. Int.*, vol. 216, no. 3, pp. 1497-1506, March 2019, <http://doi.org/10.1093/gji/ggy503>.
- [35] G.A. McMechan, "Determination of source parameters by wavefield extrapolation", *Geophys. J. Roy. Astr. S.*, vol. 71, no. 3, pp. 613-628, Dec. 1982, <https://doi.org/10.1111/j.1365-246X.1982.tb02788.x>.
- [36] G.A. McMechan, "Migration by extrapolation of time-dependent boundary values", *Geophys. Prospect.*, vol. 31, no. 3, pp. 413-420, June 1983, <https://doi.org/10.1111/j.1365-2478.1983.tb01060.x>.
- [37] A. Meléndez, J. Korenaga, V. Sallarès, A. Miniussi and C.R. Ranero, "TOMO3D: 3-D joint refraction and reflection traveltime tomography parallel code for active-source seismic data-synthetic test", *Geophys. J. Int.*, vol. 203, no. 1, pp. 158-174, Oct. 2015, <http://doi.org/10.1093/gji/ggv292>.
- [38] L. Métivier, R. Brossier, J. Virieux and S. Operto, "Full Waveform Inversion and the Truncated Newton Method", *SIAM J. Sci. Comput.*, vol. 35, no. 2, pp. B401-B437, Mar. 2013, <https://doi.org/10.1137/120877854>.
- [39] J. Morgan, M. Warner, R. Bell, J. Ashley, D. Barnes, R. Little, K. Roele and C. Jones, "Next-generation seismic experiments: wide-angle, multi-azimuth, three-dimensional, full-waveform inversion", *Geophys. J. Int.*, vol. 195, no. 3, pp. 1657-1678, Dec. 2013, <http://doi.org/10.1093/gji/ggt345>.
- [40] J. Morgan, M. Warner, G. Arnoux, E. Hooft, D. Toomey, V. Brandon and W. Wilcock, "Next-generation seismic experiments-II: wide-angle, multi-azimuth, 3-D, full-waveform inversion of sparse field data", *Geophys. J. Int.*, vol. 204, no. 2, pp. 1342-1363, Feb. 2016, <http://doi.org/10.1093/gji/ggv513>.
- [41] D.R. Muerdter, R.O. Lindsay and D.W. Ratcliff, "Imaging under edges of salt sheets: A raytracing study", *SEG Technical Program Expanded Abstracts 1996*, pp. 578-580, 1996, <https://doi.org/10.1190/1.1826707>.
- [42] M. Prada, V. Sallarès, C.R. Ranero, M.G. Vendrell, I. Grevemeyer, N. Zitellini and R. de Franco, "Seismic structure of the Central Tyrrhenian basin: geophysical constraints on the nature of the main crustal Domains", *J. geophys. Res.*, vol. 119, no. 1, pp. 52-70, Jan. 2014, <https://doi.org/10.1002/2013JB010527>.
- [43] M. Prada, F. Lavoué, M.M. Saqab, B.M. O'Reilly, S. Lebedev, J.J. Walsh and C. Childs, "Acrossaxis variations in petrophysical properties of the North Porcupine Basin, offshore Ireland: New insights from longstreamer traveltome tomography", *Basin Res.*, vol. 31, no. 1, pp. 59-76, Feb. 2019, <https://doi.org/10.1111/bre.12308>.
- [44] R.G. Pratt and M.H. Worthington, "Inverse theory applied to multi-source cross-hole tomography. Part 1: Acoustic wave-equation method", *Geophysical Prospecting EAGE*, vol. 38, no. 3, pp. 287-310, Apr. 1990, <https://doi.org/10.1111/j.1365-2478.1990.tb01846.x>.
- [45] G. Provenzano, M.E. Vardy and T.J. Henstock, "Pre-stack full waveform inversion of ultra-high-frequency marine seismic reection data", *Geophys. J. Int.*, vol. 209, no. 3, pp. 1593-1611, Jun. 2017, <https://doi.org/10.1093/gji/ggx114>.
- [46] G. Provenzano, M.E. Vardy and T.J. Henstock, "Decimetric-resolution stochastic inversion of shallow marine seismic reflection data: dedicated strategy and application to a geohazard case study", *Geophys. J. Int.*, vol. 214, no. 3, pp. 1683-1700, Sep. 2018, <https://doi.org/10.1093/gji/ggy221>.
- [47] Y. Qin and S.C. Singh, "Detailed seismic velocity of the incoming subducting sediments in the 2004 great Sumatra earthquake rupture zone from full waveform inversion of long offset seismic data", *Geophys. Res. Lett.*, vol. 44, no. 7, pp. 3090-3099, Apr. 2017, <http://doi.org/10.1002/2016GL072175>.
- [48] Y. Qin and S.C. Singh, "Insight into frontal seismogenic zone in the Mentawai locked region from seismic full waveform inversion of ultralong offset streamer data", *Geochem. Geophys. Geosy.*, vol. 19, no. 7, pp. 4342-4365, Nov. 2018, <http://doi.org/10.1029/2018GC007787>.
- [49] V. Sallarès, S. Martínez-Loriente, M. Prada, E. Gràcia, C. Ranero, M.-A. Gutscher, R. Bartolome, A. Gaïller, J.J. Dañoibeitia and N. Zitellini, "Seismic evidence of exhumed mantle rock basement at the Goringe Bank and the adjacent Horseshoe and Tagus abyssal plains (SW Iberia)", *Earth planet. Sci. Lett.*, vol. 365, no. 1, pp. 120-131, Mar. 2013, <https://doi.org/10.1016/j.epsl.2013.01.021>.
- [50] G.T. Schuster and M. Zhou, "A theoretical overview of model-based and correlation-based redatuming methods", *Geophysics*, vol. 71, no. 4, pp. S1103-S1110, Jul. 2006, <http://doi.org/10.1190/1.2208967>.
- [51] R.M. Shipp and S.C. Singh, "Two-dimensional full wavefield inversion of wide-aperture marine seismic streamer data", *Geophys. J. Int.*, vol. 151, no. 2, pp. 325-344, Nov. 2002, <https://doi.org/10.1046/j.1365-246X.2002.01645.x>.
- [52] L. Sirgue and R.G. Pratt, "Efficient waveform inversion and imaging : a strategy for selecting temporal frequencies", *Geophysics*, vol. 69, no. 1, pp. 231-248, Jan. 2004, <http://doi.org/10.1190/1.1649391>.
- [53] A. Tarantola, "Inversion of seismic reflection data in the acoustic approximation", *Geophysics*, vol. 49, no. 8, pp. 1259-1266, Aug. 1984, <http://doi.org/10.1190/1.1441754>.
- [54] D.R. Toomey, S.C. Solomon and G.M. Purdy, "Tomographic imaging of the shallow crustal structure of the East Pacific Rise at 9°30'N", *J. Geophys. Res.*, vol. 99, no. B12, pp. 24135-24157, Dec. 1994, <https://doi.org/10.1029/94JB01942>.
- [55] G. Wang, S. Yuan and S. Wang, "Retrieving Low-Wavenumber Information in FWI: An Efficient Solution for Cycle Skipping", *IEEE Geoscience and Remote Sensing Letters*, vol. 16, no. 7, pp. 1125-1129, Jul. 2019, <https://doi.org/10.1109/LGRS.2019.2892998>.
- [56] P. Wessel and W. Smith, "New version of the generic mapping tools", *EOS*, vol. 76, no. 33, pp. 329-336, Aug. 1995, <https://doi.org/10.1029/95EO00198>.
- [57] R.S. White, D. McKenzie and R.K. O'Nions, "Oceanic crustal thickness from seismic measurements and rare earth element inversions", *J. geophys. Res.*, vol. 97, no. B13, pp. 19683-19715, Dec. 1992, <https://doi.org/10.1029/92JB01749>.
- [58] P.R. Williamson, "A guide to the limits of resolution imposed by scattering in ray tomography", *Geophysics*, vol. 56, no. 2, pp. 202-207, Feb. 1991, <https://doi.org/10.1190/1.1443032>.
- [59] Z. Wu, T. Alkhalifah, Z. Zhang, F. Alonazi and M. Almalkib, "A new full waveform inversion method based on shifted correlation of the envelope and its implementation based on OPENCL", *Computers & Geosciences*, vol. 129, no. 1, pp. 1-11, Aug. 2019, <https://doi.org/10.1016/j.cageo.2019.04.007>.

- [60] C.A. Zelt and R.B. Smith, "Seismic travelttime inversion for 2-D crustal velocity structure", *Geophys. J. Int.*, vol. 108, no. 1, pp. 16-34, Jan. 1992, <https://doi.org/10.1111/j.1365-246X.1992.tb00836.x>.



Clàudia Gras Barcelona Center for Subsurface Imaging, Institute of Marine Sciences, Spanish National Research Council (CSIC), Barcelona, Spain.

Clàudia Gras Andreu received the bachelor's degree in Physics (2012), the M.Sc. degree in Reservoir Geology and Geophysics (2013) and Ph.D. (2019) degree (cum laude) from the University of Barcelona (UB), Spain. Her research interests include combining numerical and inverse techniques, as downward-continuation, travel-time tomography, and full waveform inversion, to extract high-resolution information of the subsurface. Her work at the Barcelona Center for Subsurface Imaging is devoted to the development and implementation of a generalized workflow using synthetic and field marine streamer data sets.



Clara Estela Jiménez Tejero Barcelona Center for Subsurface Imaging, Institute of Marine Sciences, Spanish National Research Council (CSIC), Barcelona, Spain.

Clara Estela Jiménez Tejero received the bachelors degree in particle physics (2004) from the University of Santiago de Compostela, Spain, the Diploma degree in experimental particle physics (2005) from the GSI Helmholtz Centre for Heavy Ion Research, Darmstadt, Germany, the M.C. degree in advance physics (2007) and the Ph.D. degree in charm hadronic theoretical physics (2012) from the University of Barcelona, Spain. Since 2013, she is holding a post-doctoral position with the Center for Subsurface Imaging, Marine Sciences Institute, Spanish National Research Council, Barcelona. Her main interest is 2D-3D waveform propagation and anisotropy, non-linear problems, downward continuation techniques of streamer data and inversion problems including 3D Travel Time Tomography and Full Adjoint Waveform inversion.



Valentí Sallarès Barcelona Center for Subsurface Imaging, Institute of Marine Sciences, Spanish National Research Council (CSIC), Barcelona, Spain.

Valentí Sallarès received the bachelors degree in physics, and the M.Sc. and Ph.D. degrees from the University of Barcelona, in 1994, 1996, and 1999, respectively. He received the García-Siñeriz Award for the Best M.Sc. and the Best Ph.D., in 1997 and 2000, respectively. He was first a Marie Curie Post-Doctoral Fellow and then a Charge de Recherche at IRD-Gosciences Azur, France. From 2005 to 2012, he was Senior Researcher at the Marine Technology Unit-CSIC, and then at Institute of Marine Sciences-ICM. He has been principal investigator of 13 competitive research projects funded by regional, national, and European funding agencies and private companies. He has authored or co-authored 70 papers in SCI journals and has over 200 communications in international meetings. He has supervised 8 PhDs. In 2020, he received the Ciutat de Barcelona Award on Environmental and Earth Sciences. His research interests include marine geophysics, especially methodological development of seismic inversion techniques and applications to study structure and active processes in continental margins.



Adrià Meléndez Barcelona Center for Subsurface Imaging, Institute of Marine Sciences, Spanish National Research Council (CSIC), Barcelona, Spain.

Adrià Meléndez received the bachelor's degree in Physics (2007) and the M.Sc. (2008) and Ph.D. (2014) degrees from the University of Barcelona. His work as a post-doctoral researcher at the Barcelona Center for Subsurface Imaging is devoted to the development of travelttime-based tools for subsurface seismic modelling. He has developed a 3-D travel-time tomographic inversion code for the joint inversion of refractions and reflections from both active and passive data, in collaboration with Yale University and Observatoire de la Cte d'Azur. Recently, he has also implemented the weak anisotropy VTI approximation for P waves to invert for the associated Thomsen's parameters.



César R. Ranero Institució Catalana de Recerca i Estudis Avanats and Barcelona Center for Subsurface Imaging, Institute of Marine Sciences, Spanish National Research Council (CSIC), Barcelona, Spain.

César R. Ranero received the Ph.D. degree from the University of Barcelona Spain in 1993 from work at the Spanish National Research Council (CSIC). From 1993 to 2005 he was a Senior Researcher with Geomar, Kiel, Germany. Since 2005 he has been an ICREA Research Professor. Since 2007 he is the Head of the Barcelona Center for Subsurface Imaging at the Marine Sciences Institute, CSIC, Barcelona. He has been a (Co-)Chief Scientist of 11 scientific cruises. He was supported by grants from the Spanish Ministry of Science, the Generalitat de Catalunya, and the European Union. He is author of over 140 peer-reviewed papers and book chapters, has organized over 20 international meetings, and delivered over 40 invited and keynote talks and seminars in Europe, America and Japan. He is a Fellow of the American Geophysical Union, a member of Academia Europaea, and has been co-awarded the Ciutat de Barcelona Earth and Environment Sciences 2019 prize.

TABLE I
RELEVANT PARAMETERS USED IN THE TTT.

Parameters	Values
Model	
Grid dimension (# nodes) (long x deep)	768 x 244
Node spacing (dx = dz)	12.5 m
Data	
Number of DC shotgathers picked	45
Distance between DC shots picked	100 m
Source and receiver depth	1 km
Maximum experimental offset	~ 5 km
Total of first arrival travel times	4,500
Inversion	
Forward star order (x,z) (node connections)	(5,5)
Eliminate data outliers with chi values	> 15
Number of iterations	10
Velocity smoothing parameter	100
Top velocity smoothing correlation lengths (x,z)	(0.1,0.1) (km)
Bottom velocity smoothing correlation lengths (x,z)	(0.5,0.25) (km)